



Effect of Spherical Polarization on the Magnetic Spectrum of the Solar Wind

Corina Dunn^{1,2} , Trevor A. Bowen¹ , Alfred Mallet¹ , Samuel T. Badman³ , and Stuart D. Bale^{1,2} ¹Space Sciences Laboratory, University of California, Berkeley, CA 94720-7450, USA; cidunn@berkeley.edu²Physics Department, University of California, Berkeley, CA 94720-7300, USA³Center for Astrophysics | Harvard & Smithsonian, Cambridge, MA 02138, USA

Received 2023 May 11; revised 2023 October 9; accepted 2023 October 15; published 2023 November 15

Abstract

Magnetic fluctuations in the solar wind are often observed to maintain constant magnitude of the magnetic field in a manner consistent with spherically polarized large-amplitude Alfvén waves. We investigate the effect of spherical polarization on the magnetic spectral index through a statistical survey of magnetic fluctuations observed by Parker Solar Probe between 20 R_{\odot} and 200 R_{\odot} . We find that deviations from spherical polarization, i.e., changes in $|\mathbf{B}|$ (compressive fluctuations) and one-dimensional discontinuities, have a dramatic effect on the scaling behavior of the turbulent fluctuations. We show that shallow $k^{-3/2}$ spectra are only observed for three-dimensional structures of constant magnetic field strength, which we identify as large-amplitude Alfvén waves. The presence of compressive fluctuations coincides with a steepening of the spectrum up to $k^{-5/3}$. Steeper power-law scalings approaching k^{-2} are observed when the fluctuations are dominated by discontinuities. Near-Sun fluctuations are found to be the most spherically polarized, suggesting that this spherical state is fundamental to the generation of the solar wind. With increasing distance from the Sun, fluctuations are found to become less three-dimensional and more compressive, which may indicate the breakdown of the Alfvénic equilibrium state.

Unified Astronomy Thesaurus concepts: Space plasmas (1544); Alfvén waves (23); Solar physics (1476); Interplanetary turbulence (830); Solar wind (1534)

1. Introduction

The solar wind is a collisionless magnetized plasma characterized by nonlinear turbulent interactions through which energy cascades from large to small scales (Bruno & Carbone 2013). The energy spectra of solar wind fluctuations typically follow power-law-type distributions; the power-law index, γ , of these fluctuations is an important diagnostic for our understanding of the relevant nonlinear processes that cascade energy from large to small scales. Equivalently, the scale dependence of the fluctuation amplitudes can be described by the scaling exponent of the second-order structure function, α_B , with $\alpha_B = -(1 + \gamma)$ for an asymptotically long inertial range. Observations from the Parker Solar Probe (PSP) mission show that the scaling of turbulent magnetic field fluctuations in the inner heliosphere is $\alpha_B = 1/2$ (Chen et al. 2020; Sioulas et al. 2023), which is consistent with three-dimensional, anisotropic turbulence (Boldyrev 2006; Chandran et al. 2015; Mallet & Schekochihin 2017). The $\alpha_B = 1/2$ scaling has often been recovered by simulations (Perez & Boldyrev 2009; Mallet et al. 2016; Chandran & Perez 2019; Meyrand et al. 2019); however, magnetic field fluctuations at 1 au typically have a steeper scaling with $\alpha_B = 2/3$ (Horbury et al. 2008; Podesta et al. 2010; Roberts 2010; Chen et al. 2013; Wicks et al. 2013).

The mode composition of the fluctuations may contribute to the observed spectral index (Podesta & Borovsky 2010; Chen et al. 2013; Bowen et al. 2018; Sioulas et al. 2023). The observed fluctuations in the solar wind exhibit characteristics consistent with large-amplitude Alfvén waves, such as high cross-helicity and constant magnetic field magnitude (Belcher et al. 1969; Goldstein et al. 1974; Lichtenstein & Sonett 1980;

Bale et al. 2019; Chaston et al. 2020; Chen et al. 2020; de Wit et al. 2020; McManus et al. 2020). This constant magnitude condition ($|\mathbf{B}| = \text{const.}$) can be described as spherical polarization, in which the magnetic field vector rotates on the surface of a sphere with radius $|\mathbf{B}|$. Measurements of the velocity fluctuations in the solar wind also show the signature of spherical polarization, further indicating the presence of large-amplitude Alfvén waves (Wang et al. 2012; Matteini et al. 2015; Raouafi et al. 2023). While strong spherical polarization is present, there are persistent subdominant fluctuations in $|\mathbf{B}|$. These compressive fluctuations are relatively poorly understood and have been attributed to a variety of sources. The magnetosonic slow mode, with small contributions from the fast mode, may make up the composition of the compressible fluctuations (Howes et al. 2012; Klein et al. 2012; Verscharen et al. 2017; Chaston et al. 2020). Pressure balance structures, the perpendicular limit of the slow mode, have also been suggested (Tu & Marsch 1995; Yao et al. 2011, 2013). The slow and fast waves may be subject to strong collisionless damping (Barnes 1966), but may be continually produced through various methods, e.g., the parametric decay instability (Derby 1978; Jayanti & Hollweg 1993; Tenerani & Velli 2013) or shearing (Roberts et al. 1992); the damping may also be suppressed in the presence of background turbulence (Meyrand et al. 2019). Chapman & Hnat (2007) suggest that the steepened spectrum at 1 au can be explained by independent scaling for the parallel (compressive) and perpendicular components of the fluctuations, where the compressive component scales with $\alpha_B = 2/3$ and the perpendicular component scales with $\alpha_B = 1/2$.

Discontinuities in the solar wind can also cause a deviation from the Alfvénic spherically polarized state (Bruno et al. 2001). One-dimensional discontinuities typically have $\alpha_B = 1$ scaling (Borovsky 2010; Li et al. 2011) and can affect the spectral index of the solar wind: the $2/3$ scaling observed at



Original content from this work may be used under the terms of the [Creative Commons Attribution 4.0 licence](https://creativecommons.org/licenses/by/4.0/). Any further distribution of this work must maintain attribution to the author(s) and the title of the work, journal citation and DOI.

1 au has been attributed to their presence (Borovsky 2010; Li et al. 2011). Intermittency in the turbulent spectra has also been attributed to discontinuities. Salem et al. (2009) used numerical methods to remove discontinuities, and recovered $\alpha_B = 2/3$, with a scaling exponent of $1/2$ for the velocity. Wu et al. (2023b) recovered monofractal scaling with $\alpha_B = 2/3$ for a near-perihelion PSP observation after numerically removing discontinuities, while Wu et al. (2023a) excluded convective structures from PSP observations from one coronal hole to obtain $\alpha_B = 1/2$. Discontinuities in the solar wind have been found to be mostly rotational, with some being tangential (Neugebauer 2006). Tangential discontinuities admit no plasma flow, while rotational ones are characterized by a large deflection of the magnetic field with no change in magnitude. Tangential discontinuities may be plasma barriers between two flux tubes (Bruno et al. 2001). Alternatively, they are the zero-width limit of pressure balance structures, which are nonpropagating structures characterized by a constant total pressure (Tu & Marsch 1995). Rotational discontinuities are typically thought to be steepened Alfvén waves (Neugebauer 2006). The magnetic “switchback” boundaries observed by Parker Solar Probe have also been analyzed as discontinuities, with similar distributions of discontinuity type to those found in the 1 au solar wind (Akhavan-Tafti et al. 2021; Larosa et al. 2021).

This work comprises a statistical survey of the magnetic field’s fluctuation geometry in order to examine the effects of deviation from the spherically polarized state on the scaling behavior. We find that steepening from $\alpha_B \approx 1/2$ to $\alpha_B \approx 2/3$ can be attributed to the presence of compressive fluctuations, while steeper structure functions up to $\alpha_B \approx 1$ are observed when fluctuations are dominated by discontinuities. The degree of spherical polarization depends on the solar distance, with fluctuations becoming less three-dimensional and more compressive. The spherical state of those observations closest to the Sun suggests that this state is fundamental to the origins of the wind.

2. Methods

Magnetometer time-series data from Encounters 1 through 8 of the Parker Solar Probe (Fox et al. 2016) Fields Experiment (FIELDS) are used, with a 1 s cadence (Bale et al. 2016). Location data for the spacecraft are from the JPL Horizons database (Giorgini 2015). Solar wind velocity data are unavailable or unreliable in many of the studied intervals and were thus excluded. We plan to analyze a reliable subset of these measurements in a future study.

Data are sorted into intervals that start every 500 s; the duration of the interval is set to equal 10 correlation times. Correlation times, $T_C(t)$, where t is the position in the time series of the start of the interval, are determined as the time it takes for the autocorrelation function, $C(t, \tau)$, to drop to $1/e$. In particular,

$$C(t, \tau) = \frac{\sum_{i=t-4000}^{t+4000} \delta \mathbf{B}(i) \cdot \delta \mathbf{B}(i + \tau)}{\sum_{i=t-4000}^{t+4000} |\delta \mathbf{B}(i)|^2}$$

$$T_C(t) = \min\{\tau: C(t, \tau) < 1/e\},$$

where δ represents the deviation from the mean—i.e., $\delta \mathbf{B}(t) = \mathbf{B}(t) - \langle \mathbf{B} \rangle$. The correlation time is estimated to the nearest 50 s. If the correlation time was greater than 5000 s, the interval was discarded, requiring a maximum interval size of 50,000 s.

Intervals were on average 10,523 s. Additionally, intervals where more than 5% of data were missing or where the magnitude squared of the magnetic field is less than 5 nT on average were discarded so that observed structures are resolvable within instrument precision. This noise threshold was varied with no significant change to the results. Any remaining NaN values are excluded from calculations. In this way, a total of 115,599 intervals are collected over the studied encounters. Results were affected minimally when nonoverlapping intervals were used—the significant overlap is chosen so that detailed statistics can be obtained at every studied solar distance. Once the correlation times are computed, we compute several parameters over each interval.

We define the compressibility of the magnetic field, C_B (Chen et al. 2020), as a ratio squared of the compressible fluctuations to the incompressible fluctuations, in particular

$$C_B = \frac{\langle \delta |\mathbf{B}|^2 \rangle}{\langle |\delta \mathbf{B}|^2 \rangle} = \frac{\sigma_{|\mathbf{B}|}^2}{\text{tr}(\mathbf{K}_B)}, \quad (1)$$

where \mathbf{K}_B is the covariance matrix of the three-component magnetic field, $\sigma_{|\mathbf{B}|}^2$ is the variance of the magnitude of the magnetic field, and angle brackets denote an average over the studied interval.

To distinguish between two- and three-dimensional structures, we develop a measure of the “three-dimensionality” of observations. We use a method similar to that employed by Bruno et al. (2001), in which the power of the variation along the directions of minimum and maximum variance is compared, but we consider only the perpendicular fluctuations because the constraint to the surface of a sphere that is relevant to spherically polarized cases limits variation to two degrees of freedom. This is accomplished by first taking the projection of the magnetic field onto the plane normal to the mean field, and then calculating the eigenvalues of the covariance matrix of the projected points. These eigenvalues represent the power in the variation in the directions of maximum and minimum perpendicular variance. We measure the perpendicular variance isotropy of each interval, Ψ , which is defined as

$$\Psi = \frac{\lambda_2}{\lambda_1 + \lambda_2}, \quad (2)$$

where λ_i are the eigenvalues. Thus, when $\Psi = 0$, variation in the perpendicular plane is in only one direction, and when $\Psi = 0.5$, variation is equally distributed along two axes. This process is illustrated for two intervals in Figure 1. We compute the Spearman correlation between Ψ and C_B as -0.097 to verify that they carry independent information about our fluctuations.

To calculate the scaling behavior of the magnetic field, the second-order structure function, $\delta \mathbf{B}^2(\tau)$, is used:

$$\delta \mathbf{B}^2(\tau) = \langle |\mathbf{B}(t + \tau) - \mathbf{B}(t)|^2 \rangle.$$

The structure function is calculated over the inertial range, using lags $20 \text{ s} < \tau < 180 \text{ s}$, averaged over the whole interval. It is then fitted versus τ in log–log space using a least-squares linear fit; the power-law scaling obtained is α_B . For an asymptotically long inertial range, this is related to the

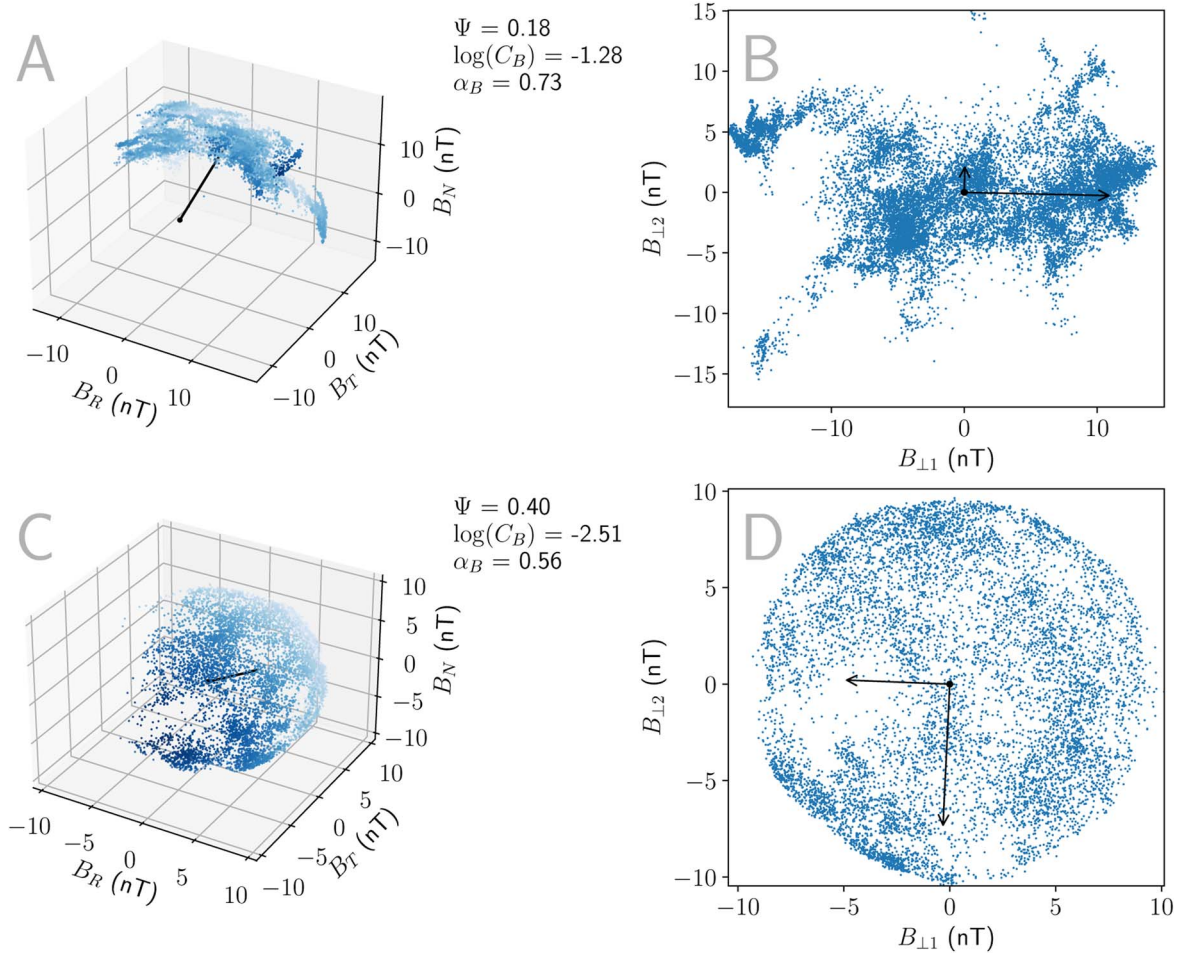


Figure 1. Panels (A) and (C) show hodograms of the magnetic field for a compressible arc-like interval (A) and for an incompressible spherically polarized interval (C). The mean field vector is shown as a black line from the origin. Panel (B) shows the perpendicular magnetic field of the structure in panel (A), with its directions of maximum and minimum variance shown as arrows scaled by the size of the corresponding eigenvalue. Panel (D) likewise shows the perpendicular magnetic field of panel (C).

magnetic spectral index, γ , by

$$\alpha_B = -(1 + \gamma).$$

3. Results

3.1. Global Statistics

Categorization by C_B and Ψ as described above yields a peaked distribution around approximately arc-polarized structures ($\Psi \simeq 0.175$; $\log(C_B) \simeq -1.35$, as estimated with a 400 bin 2D histogram), as seen in Figure 2. The compressibility was found to be uniformly small, which is consistent with past results (e.g., Chen et al. 2020) and the assumption of an Alfvénic solar wind. The mean value of C_B was found to be 0.067, representing that the compressive component was on average 26% of the amplitude of the trace fluctuations. However, the quartiles of C_B were 0.015, 0.038, and 0.085 respectively, reflecting a long-tailed distribution with most observations (68%) lower than the mean. Because $C_B \ll 1$ almost everywhere, variations in C_B are henceforth analyzed through $\log(C_B)$, shown in Figure 2(B).

Perpendicular fluctuations were also most often mainly along one axis, with a mean Ψ of 0.23, representing that 77% of the power of the variation was in the direction of maximum

perpendicular variance. Although the distribution was skewed left as seen in Figure 2(C), there were significant populations of observations exhibiting the full range of Ψ , with quartiles 0.14, 0.23, and 0.32. A total of 2.0% of observations had $\Psi > 0.45$, representing that the eigenvalue powers in the directions of minimum and maximum variance were within 5% of the total eigenvalue power of each other.

The distribution of α_B shows good agreement with previous measurements (Podesta et al. 2010; Chen et al. 2013, 2020; Bowen et al. 2018). Most data points were collected far from the Sun due to the elliptical orbit of the spacecraft, with a median radial distance of $140 R_\odot$, and the mean observed $\alpha_B = 0.65 \approx 2/3$, as we expect (Horbury et al. 2008; Podesta et al. 2010; Roberts 2010; Chen et al. 2013; Wicks et al. 2013). If data are selected from when the radial distance of the spacecraft from the Sun is $R > 200 R_\odot$, a slightly steeper mean value of $\alpha_B = 0.69$ is observed. When data from $R < 30 R_\odot$ are selected, we observe a shallow mean of $\alpha_B = 0.49$, in close agreement with previous estimates of $1/2$ (Chen et al. 2020; Sioulas et al. 2023).

Figure 2(A) also shows that the scaling behavior is a function of both Ψ and the magnetic compressibility. An $\alpha_B \approx 1/2$ structure function scaling, matching analytical models of the solar wind (Boldyrev 2006; Chandran et al. 2015; Mallet & Schekochihin 2017), is visible at low

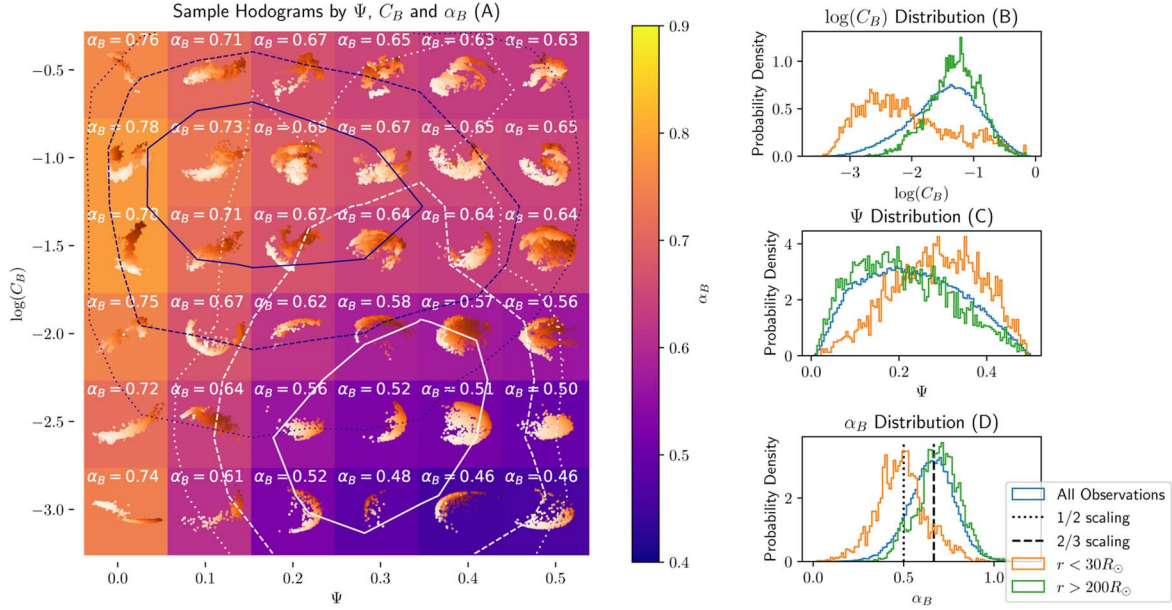


Figure 2. Panel (A): the perpendicular variance isotropy, Ψ , along the x-axis, and compressibility, $\log(C_B)$, along the y-axis, form a basis to describe the geometry of observed structures. Each depicted structure is the hodogram of an interval of the magnetic field chosen to be as close as possible in Ψ and $\log(C_B)$ values to its marked position. Hodograms are color-coded by the distance into the page, with the lightest points closest to the viewer. Each square is color-coded by the average α_B in the Ψ - C_B space contained. This α_B value is also recorded in white at the top of each square. The white and purple curves, respectively, show contours for observations inside $30 R_\odot$ and outside $200 R_\odot$. The solid, dashed, and dotted lines show, respectively, the 90th, 70th, and 50th percentiles of counts in a 100 bin 2D histogram. Panels (B), (C), and (D) show, respectively, the probability densities of $\log(C_B)$, Ψ , and α_B . The distributions of all studied intervals are shown in blue, for only data inside $30 R_\odot$ in orange, and for data outside $200 R_\odot$ in green.

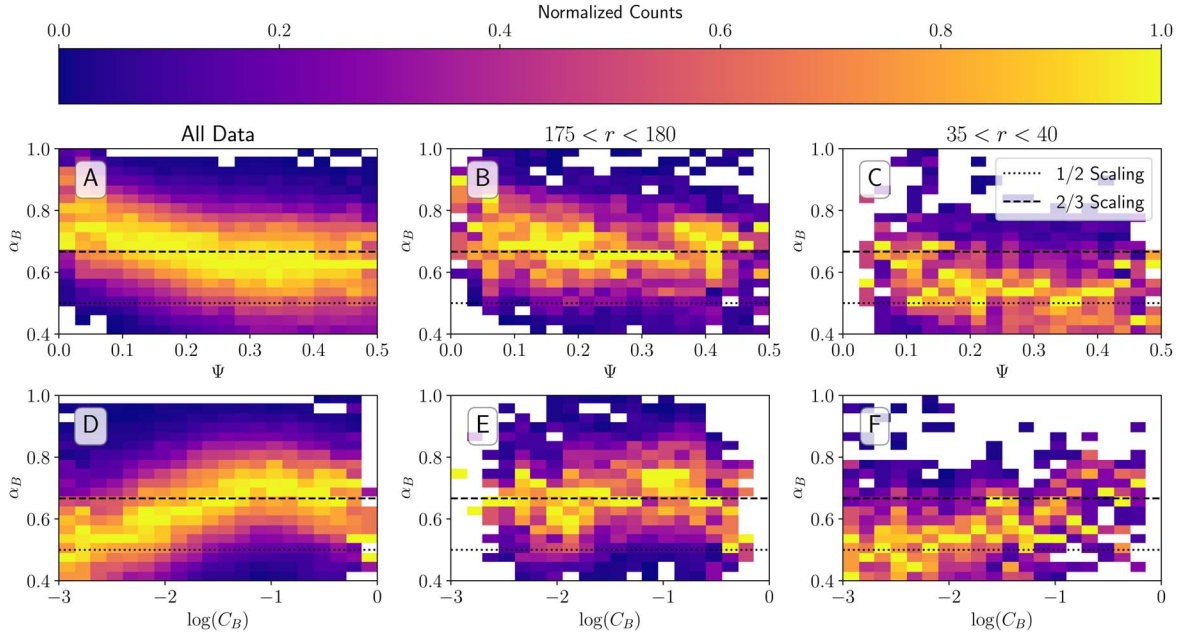


Figure 3. Panels (A), (B), and (C) show joint probability distributions of Ψ and α_B , with data column-normalized. Panels (D), (E), and (F) likewise show column-normalized joint probabilities of $\log(C_B)$ and α_B . Panels (A) and (D) show all studied data, while panels (B) and (E) show data only in a $5 R_\odot$ bin centered around $177.5 R_\odot$. Panels (C) and (F) similarly show a $5 R_\odot$ bin at $37.5 R_\odot$. The dashed black line in each panel marks 2/3 scaling, while the dotted black line marks 1/2 scaling.

compressibility ($\log(C_B) < -2$) and when $\Psi > 0.25$. These values match the characteristics of spherically polarized Alfvén waves, where the low magnetic compressibility shows that the constant magnitude condition is met.

The strongly one-dimensional structures we observe show very steep scaling (mean $\alpha_B = 0.77$ when $\Psi < 0.05$), consistent with observations of strong discontinuities, which have $\alpha_B = 1$ (Borovsky 2010; Li et al. 2011). These discontinuities would

show strong variance along one axis, causing a low Ψ . The presence of one-dimensional discontinuities in populations with low Ψ could explain the increase in α_B . The generally reported 1 au scaling, 2/3, is observed in those observations that are neither entirely one-dimensional nor of extremely low compressibility. The steeper structure functions of the more compressive observations suggest that the less Alfvénic observations have a different characteristic scaling behavior.

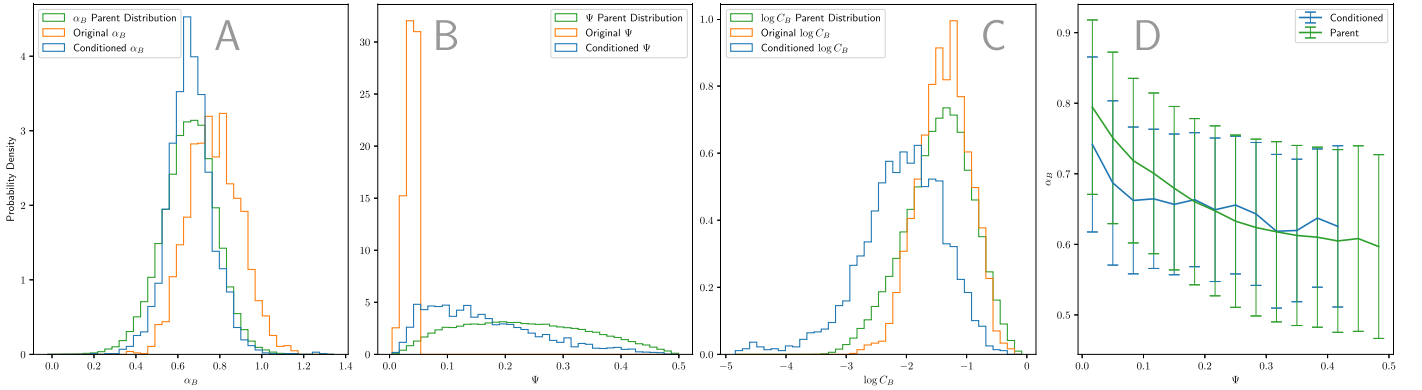


Figure 4. The figure shows the effect of the “discontinuity conditioning” described on those extremely one-dimensional observations where $\Psi < 0.05$. Panels (A), (B), and (C) show the effect on α_B , Ψ , and $\log C_B$, respectively, where orange shows unconditioned values for $\Psi < 0.05$, blue shows the conditioned distribution, and green shows the distribution for all intervals across the whole range of Ψ (the “parent distribution”). Panel (D) plots the average α_B for Ψ values in each of the 15 bins, with error bars showing the standard deviation. Conditioned α_B is plotted vs. conditioned Ψ in blue, while all unconditioned α_B values are plotted against all unconditioned Ψ values in green.

3.2. Correlation with Scaling Behavior

Correlations between Ψ and α_B and between $\log(C_B)$ and α_B are further illustrated in Figure 3. Figure 3(A) shows the correlation between α_B and Ψ . This shows an interesting saturation behavior, where α_B does not significantly decrease for $\Psi > 0.25$. This suggests that the correlation with Ψ may only be a product of discontinuities, which appear for small Ψ , and that sufficiently isotropic perpendicular fluctuations produce the same scaling exponent. Fluctuations with $\Psi \simeq 0.5$ do not have α_B distributed around the $1/2$ scaling observed in the pristine solar wind (α_B in this case is closer to $2/3$, with mean $\alpha_B = 0.59$ when $\Psi > 0.49$), suggesting that while discontinuities, or other mechanisms resulting in small Ψ , may steepen the spectrum beyond an $\alpha_B = 2/3$ scaling, these processes do not determine the evolution from $1/2$ to $2/3$ scaling observed in the solar wind. The spectral index and the magnetic compressibility are known to depend on the solar distance (Chen et al. 2020; Sioulas et al. 2023), and we will show in Figure 5(A) that Ψ does as well. We therefore consider data constrained to two narrow ranges of radial distances, shown in Figures 3(B) and (C). The trends discussed above were consistent between different radii, although α_B was generally lower for smaller radii, as expected.

However, we see a more complete range of scaling behavior when including analysis of the magnetic compressibility. Figure 3(D) shows the correlation between the log of the magnetic compressibility and α_B . Extremely incompressible intervals show $\alpha_B = 1/2$. Higher compressibility trends toward a steeper scaling with a maximum average of about $\alpha_B = 2/3$, until $\log C_B = -0.25$, at which point we see a slight negative correlation. Observations of $\log C_B > -0.25$ occur very rarely (302 times—0.3% of observations), so this apparent negative trend may simply be scatter. Figures 3(E) and (F) show the same correlation with data constrained to two narrow ranges of radial distances, confirming that the correlation between C_B and α_B is not a function of radial distance.

3.3. Impact of Discontinuities

To examine whether the trend toward steeper scaling for more one-dimensional variation is due to a changing distribution of discontinuities, we introduce an independent method of selecting and removing discontinuities. This system

of “discontinuity conditioning” is employed on the very one-dimensional intervals ($\Psi < 0.05$) to discern what characteristics they would have if no discontinuities were present. We employ nonoverlapping increments,

$$\delta B(n, \tau) = B((n+1)\tau) - B(n\tau),$$

where n is an integer, and τ is the length of the increment, which we chose to be 20 s. The distribution of these small-scale increments in each interval is examined. Outliers further than three standard deviations from the mean increment were considered to mark discontinuities. This choice of threshold did not significantly affect the resulting distributions when it was between 2σ and 4σ . These outlier increment values are then subtracted from all subsequent times in the interval, with the intent of removing the effect of each discontinuity on the structure function while preserving most of the other features of the time series. The structure function, Ψ , and C_B are then recomputed using the conditioned time series.

The conditioned distributions, which attempt to represent the background statistics of the 3009 intervals where $\Psi < 0.05$ in the absence of discontinuities, are shown in Figure 4. We see in Figure 4(A) that the distribution of α_B is shifted significantly shallower, returning reasonably closely to the distribution of all intervals (the “parent distribution”). The mean shifts from 0.77 to 0.66, comparable to the mean of 0.65 of the parent distribution. This shift suggests that steep scaling was dominated by the presence of discontinuities, consistent with Borovsky (2010) and Li et al. (2011), and that the “background” scaling for low Ψ values without a dominant discontinuity was not significantly different than the ensemble of observations for all Ψ . Similarly, we see in Figure 4(B) that the conditioned Ψ is also distributed dramatically differently. Almost the full range of Ψ values are represented, although the conditioned distribution is slightly peaked toward low Ψ . Thus, we see that the discontinuities also dominated the observed variation, where strong one-dimensional variance was almost always due primarily to these discontinuities. The remaining peak at low Ψ may indicate that one-dimensional structures also remain in the conditioned distribution. It may also be an artifact of the arbitrary threshold chosen to define discontinuities. Figure 4(D) shows the average α_B binned by Ψ for the conditioned and unconditioned data. We see that with the discontinuities removed, the relationship between the variables

Table 1
Discontinuity Type Criteria

Type	B_n Condition	$ \Delta \mathbf{B} / \mathbf{B} $ Condition
Rotational	$ B_n / \mathbf{B} \geq 0.4$	$ \Delta \mathbf{B} / \mathbf{B} < 0.2$
Tangential	$ B_n / \mathbf{B} < 0.4$	$ \Delta \mathbf{B} / \mathbf{B} \geq 0.2$
Either	$ B_n / \mathbf{B} < 0.4$	$ \Delta \mathbf{B} / \mathbf{B} < 0.2$
Neither	$ B_n / \mathbf{B} \geq 0.4$	$ \Delta \mathbf{B} / \mathbf{B} \geq 0.2$

is less pronounced. This supports the hypothesis that the increase in α_B as Ψ decreases (Figure 3(A)) is primarily due to the presence of discontinuities.

Figure 4(C) shows the change in the magnetic compressibility distribution. Observations are shown to become much less compressive, suggesting that the compressive fluctuations were dominated by these discontinuities. However, the distribution is lowered significantly past the end of the parent distribution. Given that very incompressible nondiscontinuity structures are certainly observed, it is unlikely that this distribution is a realistic representation of the compressibility of the continuous parts of these observations—this change in distribution most likely signals that the conditioning scheme does not preserve the compressive variation well. We avoid a more detailed analysis of these “conditioned” sets because significant uncertainty remains about the effects of this conditioning scheme. However, this result is a compelling confirmation that the one-dimensional fluctuations are dominated by a discontinuity that steepens the scaling.

For each of the discontinuities identified by the method above, it is then of interest what type of discontinuity we observe. The discontinuity normals are computed with minimum and maximum variance analysis (MVA) applied to the 40 s surrounding each discontinuity (Sonnerup & Scheible 1998). To improve the accuracy of MVA and avoid the effects of wave activity near the discontinuities, we only consider cases where the ratio between the intermediate and minimum eigenvalues is greater than 10 (Knetter et al. 2004), which occurred 16.1% of the time, leaving 7519 cases for analysis. Results were not significantly different than those produced using a lower threshold. We then define $|\Delta \mathbf{B}|$ as the difference in the magnitude of the field between the 60 s upstream of the discontinuity and the 60 s downstream, and $|B_n|$ as the mean magnitude of the magnetic field normal to the discontinuity. Discontinuity types are defined based on Neugebauer et al. (1984)’s classification of discontinuities as rotational, tangential, either, or neither, as listed in Table 1. This classification has also been used to understand the switchbacks observed by PSP (Akhavan-Tafti et al. 2021; Larosa et al. 2021).

Categorizing the discontinuities thus, we find 36.4% rotational discontinuities, 9.0% tangential discontinuities, 54.7% either, and 0.0% neither. The strong discontinuities we observe with $\Psi < 0.05$ are on average at $163 R_\odot$, and these proportions are similar to previous results at 1 au (see Neugebauer 2006)—past results find between 10% and 15% tangential discontinuities, between 0% and 5% neither, and the rest are split between rotational discontinuities and “either.” The high proportion of “either” designations we observe may be due to the low level of compressibility we see for the whole population, which requires that $|\Delta \mathbf{B}|/|\mathbf{B}|$ is small. We see that the discontinuities we select do not have significantly different statistics than those selected in past studies.

3.4. Radial Evolution

The spectral index is a function of radius (Chen et al. 2020; Sioulas et al. 2023), and this may be fundamentally linked to evolving fluctuation geometry. Figure 5(A) shows that fluctuations become less three-dimensional as the solar wind propagates out from the Sun, although the correlation between Ψ and the solar distance is small, with a Spearman correlation coefficient of -0.22 . More one-dimensional fluctuation could be the result of increasing numbers of discontinuities generated by nonlinear interactions. Figure 5(B) shows the radial trend of the magnetic compressibility. The wind becomes significantly more compressive outside $60 R_\odot$, then maintains a more constant value. Chen et al. (2020) reported the evolution of the magnetic compressibility as $C_B \propto r^{1.68 \pm 0.23}$, with significant scatter. Although this estimate covers the same range of values as this observation and has the same concavity, our result is not consistent with a power-law scaling. The dependence we do observe is notable for its similarity with that of the scaling exponent in Figure 5(C). The major steepening of α_B we see in this range of radii happens between $20 R_\odot$ and $60 R_\odot$, where we can see in Figure 5(A) there are very few large discontinuities present. However, the relative size of the compressive fluctuations grows significantly. Then, the increase in α_B in this range may actually be conditioned on the magnetic compressibility.

4. Conclusions

Analytic models for the scaling behavior of three-dimensional, anisotropic Alfvénic turbulence predict an $\alpha_B = 1/2$ structure function scaling (Boldyrev 2006; Chandran et al. 2015; Mallet & Schekochihin 2017). This work also recovers an approximately $1/2$ scaling exclusively when the magnetic compressibility (C_B in Equation (1)) is less than 0.01, and when the perpendicular fluctuations vary in two dimensions, with perpendicular variance isotropy (Ψ in Equation (2)) greater than 0.25. These statistics match descriptions of spherically polarized Alfvén waves. The structure function scaling is found to increase significantly to $\alpha_B \approx 1$ for structures with variation in one extremely dominant direction ($\Psi < 0.05$) (Figure 2). This steep scaling matches descriptions of the $\alpha_B = 1$ scaling of discontinuities (Borovsky 2010; Li et al. 2011). Upon numerically removing discontinuities from these low- Ψ intervals, we find that the conditioned data sets have an underlying scaling behavior similar to the parent distribution, confirming that this steep scaling can be attributed to the presence of a large discontinuity (Figure 4). The observed one-dimensional variation itself is also found by this scheme to be mainly due to these discontinuities. We categorize the discontinuities we find, which are on average at $163 R_\odot$, as 36.4% rotational, 9.0% tangential, 54.7% either, and 0.0% neither. These proportions are similar to previous results at 1 au (Neugebauer 2006). Thus, the strong, steeply scaling, one-dimensional variation we observe matches previous descriptions of discontinuities in the solar wind.

Decreased Ψ is associated with very steep ($\alpha_B > 2/3$) scaling, and when Ψ is increased, the mean α_B decreases. However, even when $\Psi > 0.49$, the mean $\alpha_B = 0.59 > 1/2$. This suggests that the distribution of discontinuities, or some other mechanism that increases Ψ , cannot fully explain the behavior of the magnetic scaling exponent, because a high Ψ , which we interpret as indicating the absence of discontinuities,

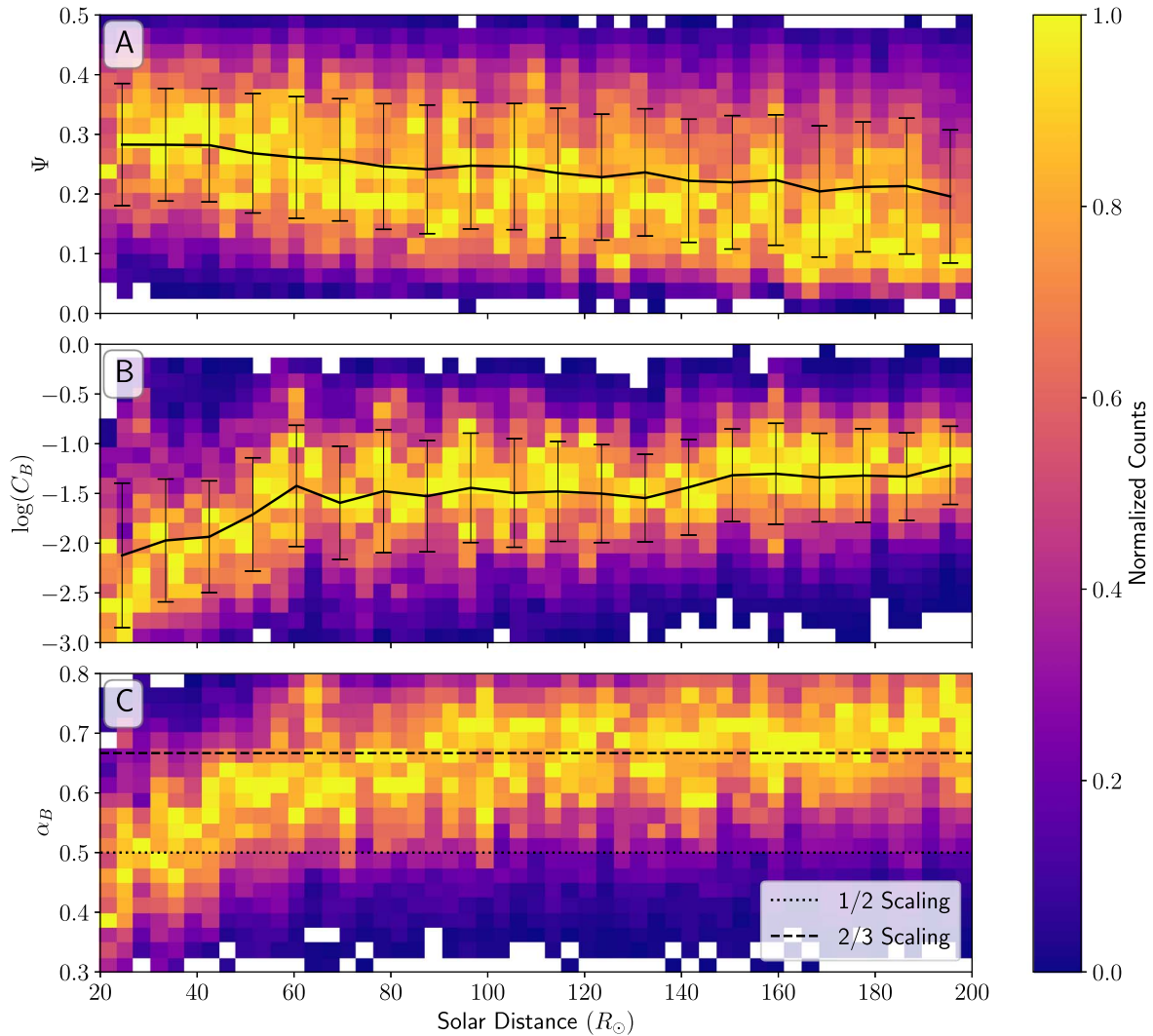


Figure 5. Panel (A) shows the evolution of Ψ with solar distance as a column-normalized joint probability. Panel (B) shows a column-normalized joint probability between the solar distance and $\log(C_B)$. In Panels (A) and (B), the average values in 10 R_\odot bins of Ψ and $\log(C_B)$, respectively, are plotted in black, with error bars giving the standard deviation in each bin. Panel (C) shows a column-normalized joint probability between the solar distance and α_B , with dashed and dotted black lines indicating, respectively, 2/3 and 1/2 scalings.

does not result in the $\alpha_B = 1/2$ scaling observed closer to the Sun (Figure 3(A)). In addition to the effect of discontinuities, the structure function scaling is found to be conditioned by the magnetic compressibility. Incompressible fluctuations with $C_B < 0.01$ are found to have $\alpha_B \lesssim 1/2$, with more compressible structures associated with $\alpha_B \approx 2/3$ (Figure 3(D)). This steeper scaling for compressible structures may be due to an independent parallel component of the magnetic field with steeper scaling, which is consistent with the result of Chapman & Hnat (2007) for the velocity fluctuations. The compressive fluctuations could be small-amplitude tangential discontinuities, which are known to have steep scaling (Tu & Marsch 1995). Alternatively, the compressive fluctuations are often attributed to the magnetosonic slow mode (Howes et al. 2012; Klein et al. 2012; Verscharen et al. 2017), which is coupled to the Alfvén mode by the parametric decay instability (Derby 1978; Jayanti & Hollweg 1993; Tenerani & Velli 2013). Nonlinear energy exchange between the slow and Alfvén modes may then affect the scaling behavior. To summarize, our result suggests that an $\alpha = 1/2$ scaling is only possible when there are no compressive fluctuations present and that

an $\alpha = 1$ scaling is only observed in the presence of strong discontinuities.

Many previous authors have also observed that α_B increases from 1/2 in the inner heliosphere to 2/3 outside about 60 R_\odot (Podesta et al. 2010; Roberts 2010; Wicks et al. 2013; Chen et al. 2020). We observe that Ψ is also correlated with solar distance, with Ψ decreasing as the solar wind streams out from the Sun (Figure 5). This may be a function of the increasing importance of discontinuities. As mentioned above, the behavior of Ψ is strongly controlled by the presence or absence of discontinuities. We may also be seeing some process that progressively destroys three-dimensional, spherically polarized Alfvén waves, for example, reflections or the parametric decay instability.

The magnetic compressibility also monotonically increases with radius. The very low C_B we observe at small radii suggests that the primordial state of fluctuations in the corona is that of three-dimensional, spherically polarized Alfvén waves. The steepening of α_B that we see between 10 and 60 R_\odot coincides with a large increase in C_B . Given that the corresponding measurements of Ψ show that large discontinuities were rare in this range, the increase in compressibility may be a major factor in the increase of α_B . The

mechanism for the growth in the compressive fluctuations depends on their nature. The increase in compressibility may be caused by an increased distribution of tangential discontinuities, which could be increasingly generated from pressure balance structures. If the compressive fluctuations are dominated by the slow mode, we may be seeing an in-situ generation mechanism, e.g., the parametric decay instability of Alfvén waves. The compressibility is intimately connected with the Alfvénicity and may serve as a proxy for the cross-helicity, which has previously been shown to be related to the spectral index (Podesta & Borovsky 2010; Chen et al. 2013; Bowen et al. 2018; Sioulas et al. 2023). So, we can see the increase in compressibility as a breakdown of an Alfvénic equilibrium state, which coincides with spectral steepening. A study of the velocity fluctuations of the solar wind would lend insight into the relationship between C_B , the cross-helicity, and the residual energy, and would reveal whether the velocity spectrum is similarly dependent on the compressibility.

Our observations may also be important in understanding the radial evolution of the constant magnitude “switchbacks” of the magnetic field that have been historically noted in various spacecraft data (Balogh et al. 1999; Neugebauer & Goldstein 2013) and are ubiquitous in the PSP data (Bale et al. 2019; Kasper et al. 2019; de Wit et al. 2020; Horbury et al. 2020; Raouafi et al. 2023). These structures are inherently associated with a constant- $|B|$ state (Raouafi et al. 2023), and observation of increased compressibility may be a signature of the decay of switchbacks via parametric decay (Tenerani et al. 2021) or other mechanisms. Furthermore, discontinuities observed at larger heliospheric distances are more compressible than the discontinuities observed in the inner heliosphere, which may suggest the growth of pressure-balanced structures or other non-Alfvénic boundaries rather than Alfvénic switchback rotations (Larosa et al. 2021). Switchbacks are thought to interact with the turbulent cascade of the solar wind (Bourouaine et al. 2020; Martinović et al. 2021), and a comprehensive study of switchback properties and their relationship with C_B , ψ , and α_B through the inner heliosphere may provide a significant constraint on the evolution of switchbacks and their relation to turbulence in the solar wind.

Acknowledgments

C.D. is supported by NASA PSP-GI grant No. 80NSSC21K1771 as well as by PSP FIELDS funding through NASA Contract No. NNN06AA01C.

Software: numpy (Harris et al. 2020), scipy (Virtanen et al. 2020), matplotlib (Hunter 2007), pandas (The pandas development team 2020), sunpy (The SunPy Community et al. 2020), astropy (Astropy Collaboration 2022).

ORCID iDs

Corina Dunn  <https://orcid.org/0009-0007-8306-2635>
Trevor A. Bowen  <https://orcid.org/0000-0002-4625-3332>
Alfred Mallet  <https://orcid.org/0000-0001-9202-1340>
Samuel T. Badman  <https://orcid.org/0000-0002-6145-436X>
Stuart D. Bale  <https://orcid.org/0000-0002-1989-3596>

References

Akhavan-Tafti, M., Kasper, J., Huang, J., & Bale, S. 2021, *A&A*, **650**, A4
Astropy Collaboration, Price-Whelan, A. M., Lim, P. L., et al. 2022, *ApJ*, **935**, 167
Bale, S., Badman, S., Bonnell, J., et al. 2019, *Natur*, **576**, 237
Bale, S., Goetz, K., Harvey, P., et al. 2016, *SSRv*, **204**, 49

Balogh, A., Forsyth, R., Lucek, E., Horbury, T., & Smith, E. 1999, *GeoRL*, **26**, 631
Barnes, A. 1966, *PhFI*, **9**, 1483
Belcher, J., Davis, L., Jr., & Smith, E. 1969, *JGR*, **74**, 2302
Boldyrev, S. 2006, *PhRvL*, **96**, 115002
Borovsky, J. E. 2010, *PhRvL*, **105**, 111102
Bourouaine, S., Perez, J. C., Klein, K. G., et al. 2020, *ApJL*, **904**, L30
Bowen, T. A., Mallet, A., Bonnell, J. W., & Bale, S. D. 2018, *ApJ*, **865**, 45
Bruno, R., & Carbone, V. 2013, *LRSP*, **10**, 2
Bruno, R., Carbone, V., Veltri, P., Pietropaolo, E., & Bavassano, B. 2001, *P&SS*, **49**, 1201
Chandran, B. D., & Perez, J. C. 2019, *JPhI*, **85**, 905850409
Chandran, B. D., Schekochihin, A. A., & Mallet, A. 2015, *ApJ*, **807**, 39
Chapman, S., & Hnat, B. 2007, *GeoRL*, **34**, L17103
Chaston, C., Bonnell, J., Bale, S., et al. 2020, *ApJS*, **246**, 71
Chen, C., Bale, S., Bonnell, J., et al. 2020, *ApJS*, **246**, 53
Chen, C., Bale, S., Salem, C., & Maruca, B. 2013, *ApJ*, **770**, 125
Derby, N. F., Jr 1978, *ApJ*, **224**, 1013
de Wit, T. D., Krasnoselskikh, V. V., Bale, S. D., et al. 2020, *ApJS*, **246**, 39
Fox, N., Velli, M., Bale, S., et al. 2016, *SSRv*, **204**, 7
Giorgini, J. D. 2015, *IAUGA*, **29**, 2256293
Goldstein, M. L., Klimas, A. J., & Barish, F. D. 1974, in *Solar Wind Three: Proc. of the Third Conference: On the Theory of Large Amplitude Alfvén Waves*, ed. C. P. Sonett, P. J. Coleman, Jr., & J. M. Wilcox (Dordrecht: Reidel), 385
Harris, C. R., Millman, K. J., van der Walt, S. J., et al. 2020, *Natur*, **585**, 357
Horbury, T. S., Forman, M., & Oughton, S. 2008, *PhRvL*, **101**, 175005
Horbury, T. S., Woolley, T., Laker, R., et al. 2020, *ApJS*, **246**, 45
Howes, G., Bale, S., Klein, K., et al. 2012, *ApJL*, **753**, L19
Hunter, J. D. 2007, *CSE*, **9**, 90
Jayanti, V., & Hollweg, J. V. 1993, *JGR*, **98**, 19049
Kasper, J. C., Bale, S. D., Belcher, J. W., et al. 2019, *Natur*, **576**, 228
Klein, K., Howes, G., TenBarge, J., et al. 2012, *ApJ*, **755**, 159
Knetter, T., Neubauer, F., Horbury, T., & Balogh, A. 2004, *JGRA*, **109**, A06102
Larosa, A., Krasnoselskikh, V., de Wit, T. D., et al. 2021, *A&A*, **650**, A3
Li, G., Miao, B., Hu, Q., & Qin, G. 2011, *PhRvL*, **106**, 125001
Lichtenstein, B., & Sonett, C. 1980, *GeoRL*, **7**, 189
Mallet, A., Schekochihin, A., Chandran, B., et al. 2016, *MNRAS*, **459**, 2130
Mallet, A., & Schekochihin, A. A. 2017, *MNRAS*, **466**, 3918
Martinović, M. M., Klein, K. G., Huang, J., et al. 2021, *ApJ*, **912**, 28
Matteini, L., Horbury, T., Pantellini, F., Velli, M., & Schwartz, S. 2015, *ApJ*, **802**, 11
McManus, M. D., Bowen, T. A., Mallet, A., et al. 2020, *ApJS*, **246**, 67
Meyrand, R., Kanekar, A., Dorland, W., & Schekochihin, A. A. 2019, *PNAS*, **116**, 1185
Neugebauer, M. 2006, *JGRA*, **111**, A04103
Neugebauer, M., Clay, D., Goldstein, B., Tsurutani, B., & Zwickl, R. 1984, *JGR*, **89**, 5395
Neugebauer, M., & Goldstein, B. E. 2013, in *AIP Conf. Proc 1539, SOLAR WIND 13: Proceedings of the Thirteenth International Solar Wind Conference*, ed. G. P. Zank (Melville, NY: AIP), 46
Perez, J. C., & Boldyrev, S. 2009, *PhRvL*, **102**, 025003
Podesta, J., & Borovsky, J. 2010, *PhFI*, **17**, 112905
Podesta, J., Borovsky, J., & Gary, S. 2010, *ApJ*, **712**, 685
Raouafi, N., Matteini, L., Squire, J., et al. 2023, *SSRv*, **219**, 8
Roberts, D. A. 2010, *JGRA*, **115**, 12101
Roberts, D. A., Goldstein, M. L., Matthaeus, W. H., & Ghosh, S. 1992, *JGR*, **97**, 17115
Salem, C., Mangeney, A., Bale, S. D., & Veltri, P. 2009, *ApJ*, **702**, 537
Sioulas, N., Huang, Z., Shi, C., et al. 2023, *ApJL*, **943**, L8
Sonnerup, B. U., & Scheible, M. 1998, *ISSIR*, **1**, 185
Tenerani, A., Sioulas, N., Matteini, L., et al. 2021, *ApJL*, **919**, L31
Tenerani, A., & Velli, M. 2013, *JGRA*, **118**, 7507
The pandas development team, 2020 pandas-dev/pandas: Pandas, 1.2.4, Zenodo, doi:10.5281/zenodo.3509134
The SunPy Community, Barnes, W. T., Bobra, M. G., et al. 2020, *ApJ*, **890**, 68
Tu, C.-Y., & Marsch, E. 1995, *SSRv*, **73**, 1
Verscharen, D., Chen, C. H., & Wicks, R. T. 2017, *ApJ*, **840**, 106
Virtanen, P., Gommers, R., Oliphant, T. E., et al. 2020, *NatMe*, **17**, 261
Wang, X., He, J., Tu, C., et al. 2012, *ApJ*, **746**, 147
Wicks, R. T., Roberts, D. A., Mallet, A., et al. 2013, *ApJ*, **778**, 177
Wu, H., He, J., Huang, S., et al. 2023a, *ApJ*, **947**, 45
Wu, H., Huang, S., Wang, X., et al. 2023b, *ApJL*, **947**, L22
Yao, S., He, J.-S., Marsch, E., et al. 2011, *ApJ*, **728**, 146
Yao, S., He, J.-S., Tu, C.-Y., Wang, L.-H., & Marsch, E. 2013, *ApJ*, **774**, 59